# Characterization of Different Osteosarcoma Phenotypes by PET Imaging in Preclinical Animal Models

Carmen Campanile[1], Matthias J.E. Arlt[1], Stefanie D. Krämer[2], Michael Honer[3], Ana Gvozdenovic[1], Patrick Brennecke[1], Cindy R. Fischer[2], Adam A. Sabile[1], Adrienne Müller[2], Simon M. Ametamey[2], Walter Born[1], Roger Schibli[2], and Bruno Fuchs[1]

[1]Laboratory for Orthopaedic Research, Department of Orthopaedics, Balgrist University Hospital, Zurich, Switzerland; [2]Radiopharmaceutical Sciences, Institute of Pharmaceutical Sciences, Department of Chemistry and Applied Biosciences of ETH Zurich, Switzerland; and [3]F. Hoffmann-La Roche, Basel, Switzerland

The aim of this study was to characterize the different phenotypes of osteosarcoma by PET, comparing the uptake of 3 tracers ([18F]-FDG, [18F]-fluoromisonidazole [[18F]-FMISO], and [18F]-fluoride) in preclinical mouse models that reflect the heterogeneity of the human disease. **Methods:** Mouse LM8 osteosarcoma, human 143B, and Caprin-1 stably overexpressing SaOS-2 cells were injected intratibially in C3H and severe-combined immunodeficient mice. PET imaging with [18F]-FDG, [18F]-FMISO, and [18F]-fluoride was performed in these mouse models, and a ratio between the standardized uptake value of the primary tumor and a control area of bone was calculated and compared among the models. Histology and immunohistochemistry were performed to confirm the PET findings. **Results:** The pattern of tracer uptake differed among the primary tumors of the 3 models in accordance with the histology and immunohistochemistry on primary tumor sections. The osteolytic tumors in the 143B model showed the highest uptake of [18F]-FDG, an indicator of glucose metabolism, which was significantly higher ($P < 0.05$) than in the SaOS-2/Caprin-1 model and correlated with the percentage of Ki67-positive cells in the primary tumors. Hypoxia, indicated by [18F]-FMISO accumulation, was higher in the SaOS-2/Caprin-1 and 143B cell line–derived tumors ($P < 0.01$). Finally [18F]-fluoride, a marker of bone remodeling, correlated with the osteoblastic phenotype. The SaOS-2/Caprin-1 cell–derived tumors showed a significantly higher uptake than the moderately osteoblastic LM8 ($P < 0.05$) and the osteolytic 143B ($P < 0.01$) cell line–derived tumors. **Conclusion:** Differential PET imaging with tracers indicating metabolic activity, hypoxia, or bone remodeling will be helpful for the characterization of different osteosarcoma phenotypes and subsequent evaluation of more specific treatment modalities targeting the processes that are predominant in each specific tumor type or subtype.

**Key Words:** osteosarcoma; positron emission tomography; osteoblastic; osteolytic

Osteosarcoma is the most common primary bone tumor, occurring most frequently in adolescents between the ages of 15 and 19 y (*1*). Its progression is strongly affected by the imbalance between osteoclasts and osteoblasts that results radiologically in an osteolytic or an osteoblastic phenotype or, in most of the cases, a mixture of both (*2*). Primary tumors predominantly occur in long bones—for example, the distal femur (31.5%), the proximal tibia (15.2%), and the proximal humerus (9%)—and metastases are predominantly found in the lung and to a lesser extent bone (*3*).

In the late 1970s, the combination of surgery and neoadjuvant chemotherapy increased the 5-y survival rate of osteosarcoma patients with localized disease from 15%–20% to 50%–70% (*3,4*). In 2005, a new international project (European and American Osteosarcoma Study) was started with the final aim of refining the treatment practice by stratifying the patients after primary tumor resection (*4*). So far, the most valuable prognostic factors in osteosarcoma are the presence of metastases and the response to chemotherapy, but these observations do not give any information about the deregulated processes occurring in the tumor (*5*). Consequently, in the recent years, clinical research focused on selecting and improving tools with a prognostic value for the evaluation of the biologic processes affecting the tumor growth, key for the optimization of treatment efficacy. In this context, distinct and improved imaging procedures might also be helpful to obtain already at the time of diagnosis information on deregulated processes within the primary tumor without the need of an invasive intervention.

Radiography and CT and MR imaging that are used in osteosarcoma diagnosis and management are not associated with any prognostic feature (*6*). PET, instead, has proven to be a reliable prognostic factor in the last few years in various tumors when used during or after treatment. Weber et al. demonstrated that 35% or more reduced standardized uptake value (SUV) after the first cycle of chemotherapy was associated with a better prognosis and longer overall survival of patients with gastroesophageal cancer imaged with [18F]-FDG (*7*). Along the same line, Benz et al. confirmed that a cutoff of 35% SUV reduction was predictive of a good response in patients with high-grade soft-tissue sarcomas imaged with [18F]-FDG (*8*). Consistent with these studies, Kim et al. showed that in patients with osteosarcoma or with the Ewing sarcoma family of tumors [18F]-FDG PET can be used for the assessment of the response to chemotherapy before surgery. Indeed, they

observed a significant correlation ($P < 0.01$) between the histologic response and the difference in SUV before and after chemotherapy (9). Complementary information on the biology of individual tumors is accessible by multitracer imaging, as demonstrated, for instance, by Eary et al. for soft-tissue sarcoma (10).

On the basis of these results, in our study we explored the potential usefulness of additional PET probes, besides ^{18}F-FDG, for the characterization of the heterogeneous biology of different osteosarcoma phenotypes to obtain information on prevailing biologic processes, before different regimens of drug treatment are started. To achieve this aim, we took advantage of 3 mouse models of osteosarcoma with a well-defined phenotype from osteolytic to osteoblastic that were scanned with a variety of PET tracers. Tracer accumulation was interpreted using the known phenotype. Translated to a clinical setting, this may in the future provide information before treatment and consequently direct the choice of a therapeutic protocol depending on the biologic processes that are predominant. In the present study, we selected 3 tracers that target different metabolic processes, which strongly affect osteosarcoma development: ^{18}F-FDG, ^{18}F-FMISO, and ^{18}F-fluoride. In general, osteosarcoma is characterized by a high metabolic rate and consequently high ^{18}F-FDG uptake (11). A differential uptake can be expected among the types and subtypes of osteosarcoma depending on their growth rate. Franzius et al. reported no differences in tumor uptake among the subtypes of the conventional-type osteosarcoma—that is, osteoblastic, fibroblastic, and chondroblastic—however, no reports are found evaluating possible differences in ^{18}F-FDG uptake among the different types of osteosarcoma (12). ^{18}F-FMISO is an indicator of hypoxia that diffuses passively into cells and is retained only in hypoxic areas after a 2-electron reduction reaction (13). It is well established that hypoxia is associated with aggressive tumor phenotype and with pronounced chemoresistance dependent on the higher expression and stabilization of the heterodimeric hypoxia-inducible factor complex and on the overexpression of direct targets such as carbonic anhydrase IX (CaIX), which is associated with worse prognosis and lower survival in several tumors (13,14). In osteosarcoma, high levels of hypoxia-inducible factor 1α in tumor tissue and a high serum level of the transcription product of its target gene, vascular endothelial growth factor, are associated with a poor prognosis (15,16). Therefore, information about the hypoxia extent in the tumor provides important information about the responsiveness of the tumor to the chemotherapy and for tumor-tailored treatment (17). Much like ^{18}F-FDG, it was shown that ^{18}F-FMISO exhibits predictive power for chemotherapy success in non–small cell lung and head and neck cancers. A differential uptake of ^{18}F-FMISO is expected, considering that the response to chemotherapy in osteosarcoma patients strongly depends on the level of hypoxia. The third tracer that we selected in this study was ^{18}F-fluoride, which specifically targets tumors undergoing bone-remodeling processes because it replaces hydroxyl groups during the formation of hydroxyapatite and thereby indicates osteoblastic mineralization. Data on the predictive power of ^{18}F-fluoride for the outcome of bone tumors have so far not been published. However, information about the predominance of lytic or blastic lesions is decisive for a more selective and efficient treatment strategy (18).

The data of the present study provide more detailed information on the use of ^{18}F-FDG, ^{18}F-FMISO, and ^{18}F-fluoride for assessing tumor metabolism, tumor aggressiveness in terms of chemoresistance, and whether the tumor cellular phenotype is either predominantly osteoblastic or osteoclastic.

## MATERIALS AND METHODS

### Cell Lines

The human osteosarcoma cell line 143B was obtained from the European Collection of Cell Cultures, human SaOS-2 cells stably transfected with malignancy-enhancing Caprin-1 and a neomycin-resistance gene were generated in our laboratory by Dr. Adam A. Sabile (19), and murine LM8 osteosarcoma cells were a kind gift from Takafumi Ueda. Cells were cultured in Dulbecco modified Eagle medium–HamF12 (1:1) medium (PAA GmbH) supplemented with 10% fetal calf serum (tissue culture medium) as described by Arlt et al. (20). SaOS-2 cells transfected with Caprin-1 were grown in tissue culture medium containing Neomycin (0.6 mg/mL; Invitrogen).

### Animal Models

Animal care was done in accordance with the Swiss Animal Welfare legislation, and the experiments were approved by the Veterinary Office of the Canton Zurich. Six- to 8-wk-old female immunosuppressed severe combined immunodeficient and immunocompetent C3H mice were purchased from Charles River Laboratories and kept under pathogen-free conditions. Tumor cells used for intratibial injection into mice were detached with trypsin–ethylenediaminetetraacetic acid (EDTA), washed twice with phosphate-buffered saline containing 0.05% EDTA, and resuspended in phosphate-buffered saline–EDTA at a final density of $5 \times 10^7$ cells/mL. A 10-μL aliquot of the cell suspension was orthotopically injected into the medullar cavity of the left tibia of the mice as previously described (21).
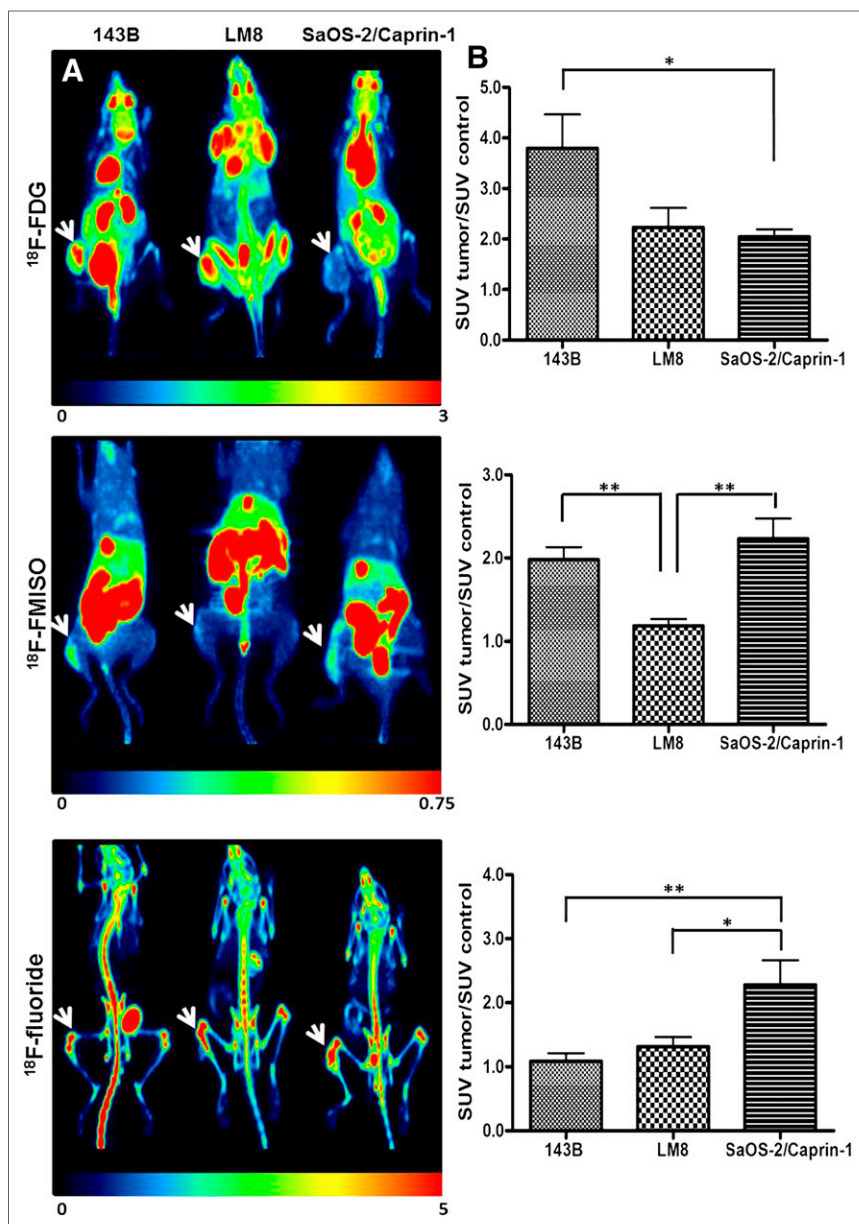
The 143B cell–injected mice were sacrificed between days 21 and 23 after tumor cell inoculation (i.e., after the last PET scan), LM8 cell–injected mice on day 27, and SaOS-2/Caprin-1 cell–injected animals between days 61 and 115 after tumor cell inoculation.

### PET Scans

Animals were transported to the PET facility for acclimatization 5–7 d before the first PET scan. Radiotracers were produced as described in the supplemental data (available online only at http://jnm.snmjournals. org). ^{18}F-FDG (9.5–16.4 MBq), ^{18}F-FMISO (16.1–44.6 MBq), or ^{18}F-fluoride (20.4–46.7 MBq) was injected in a 100-μL final volume into a lateral tail vein in awake mice (except for during ^{18}F-FDG scanning, for which 143B and SaOS-2/Caprin-1 mice were anesthetized). ^{18}F-FDG was injected 30 min before the scan start, and ^{18}F-fluoride and ^{18}F-FMISO were injected 90 min before the scan start. Ten minutes before scan start, mice were anesthetized in an incubation chamber containing 5% isoflurane (Abbott) in a mixture (1/1) of air and oxygen. To reduce the muscle and brown fat uptake of ^{18}F-FDG in 143B and SaOS-2/Caprin-1 mice, anesthesia with isoflurane was initiated on a heating pad at 37°C (Harvard Apparatus) 10 min before ^{18}F-FDG injection. PET whole-body images were acquired on a Vista eXplore preclinical PET/CT scanner (Sedecal; 4.8-cm axial field of view) with 2 bed positions, 15-min acquisition per position starting with the upper body. During the scans, the mice were kept anesthetized with 2%–3% isoflurane in air/oxygen (200 mL/min each) and monitored as reported (22). PET was followed by CT scanning in selected experiments. Each animal underwent up to 2 PET scans with different tracers, with minimal recovery times of 24 h. The reconstruction and coronal images were obtained in a manner as described in the study by Mumprecht et al. (23). Coronal images in false colors were obtained with the PMOD software (PMOD Technologies Ltd.). For direct comparison, the color scales were normalized to injected radioactivity dose and body weight of the animal to reveal the SUV.

### Quantitative Analysis and Calculation of Sensitivity

PET images were analyzed by manual selection of the volume of interest containing the tumor. For the reference volume of interest (no tumor), the tumor volume of interest was mirrored (sagittal) on a control

**FIGURE 1.** Quantitative analysis of PET tracer uptake in indicated osteosarcoma mouse models. Tracer uptake was estimated as ratio between SUV in tumor leg and SUV in control leg between 21 and 115 d after tumor cell injection, depending on growth rate of individual tumors. Representative PET images obtained with indicated tracers and described animal models (A) and quantitative analysis (B) are shown. SUV scale bar, 0–3 for $^{18}$F-FDG, 0–0.75 for $^{18}$F-FMISO, 0–5 for $^{18}$F-fluoride. Arrows indicate tumor cell injection sites. Number of mice: $^{18}$F-FDG, n = 4 in 143B model, n = 6 in LM8 model, and n = 5 in SaOS-2/Caprin-1 model; $^{18}$F-fluoride, n = 15 in 143B model, n = 8 in LM8 model, and n = 4 in SaOS-2/Caprin-1 model; $^{18}$F-FMISO, n = 15 in 143B model, n = 7 in LM8 model, and n = 5 in SaOS-2/Caprin-1 model. *P < 0.05. **P < 0.01.

bone. For mice with LM8 cell–derived tumors, a detailed description of the protocol used for the quantitative analysis is provided in Supplemental Figure 1. The average radioactivity concentrations in the tumor and reference region were expressed as SUV, and their ratios were calculated and compared in the 3 osteosarcoma mouse models. Mice with high spillover from radioactivity in the urinary bladder were excluded from the analysis. The sensitivity was defined as the percentage of mice in individual experimental groups with a detectable tumor in the PET imaging slices selected by visual inspection by 2 independent masked researchers.

### Histology and Immunohistochemistry

After the mice were sacrificed, intratibial primary tumors were collected, fixed in 4% paraformaldehyde, treated with decalcifying agent (Osteosoft; Merck Chemicals) for 1 wk, and embedded in paraffin for histologic and immunohistochemical staining. To compare the PET imaging results with immunohisto-chemistry and histology, we used immunore-active Ki67 in tumor tissue sections as a marker of proliferation, CaIX as a marker of hypoxia, and Goldner trichrome (Carl Roth GmbH) staining for histology. Tumor sections of 6 μm were analyzed: Goldner tri-chrome staining was done according to the instructions of the provider; Ki67 was immunostained with rabbit polyclonal Ki67 antibody (Abcam) and CaIX with rabbit poly-clonal CaIX antibody (Novus Biologicals Ltd.). Immunostaining was visualized with peroxidase-conjugated secondary antibodies (Vector Laboratories Inc.), Vectastain Elite ABC (Vector Laboratories Inc.), and a sub-strate-chromogen system (Dako). The quantifi-cation procedure for the staining is described in section 3 of the supplemental data.

### Statistics

Statistical analysis was performed with GraphPad Prism (version 5.01, Network soft-ware; GraphPad Software). The ratios be-tween the tumor and the control SUVs were compared among the 3 osteosarcoma models by 2-tailed Student t test. P values less than 0.05 were considered as statistically signifi-cant and less than 0.01 as highly statistically significant. The SUVs in Table 1 are indi-cated as the mean ± SEM.

### RESULTS

#### PET Imaging of Intratibial Osteosarcoma

To address the heterogeneity of osteosar-coma phenotypes, 3 distinct osteosarcoma mouse models were investigated in this study (section 4, supplemental data; Supple-mental Fig. 4).

$^{18}$F-FDG. Tumor-selective higher $^{18}$F-FDG uptake, compared with control tissue—indicating high glucose metabolism—was detectable in the primary tumors of all 3 osteosarcoma mouse models and defined the margins of the tumor (Fig. 1A). The mean SUVs of tumor and control regions are shown in Table 1. The osteolytic 143B cell line–derived tumors showed the highest $^{18}$F-FDG uptake, with a 3.79 ± 0.67-fold higher accumulation in the tumor than in the control region of the healthy leg. The LM8 cell line–derived mildly osteoblastic tumors showed a 2.22 ± 0.39-fold higher tracer uptake in the tumor than in the control hip region. Tumors derived from SaOS-2/Caprin-1 cells showed the lowest $^{18}$F-FDG

## TABLE 1
### Absolute SUVs

| Mouse model | $^{18}$F-FDG SUV | $^{18}$F-FMISO SUV | $^{18}$F-Fluoride SUV |
|---|---|---|---|
| 143B control | 0.357 ± 0.077 | 0.156 ± 0.009 | 2.045 ± 0.250 |
| 143B | 1.36 ± 0.239 | 0.309 ± 0.023 | 2.217 ± 0.262 |
| LM8 control | 0.397 ± 0.062 | 0.142 ± 0.006 | 1.554 ± 0.14 |
| LM8 | 0.884 ± 0.155 | 0.168 ± 0.011 | 2.045 ± 0.232 |
| SaOS-2/Caprin-1 control | 0.293 ± 0.026 | 0.142 ± 0.024 | 0.951 ± 0.227 |
| SaOS-2/Caprin-1 | 0.598 ± 0.044 | 0.317 ± 0.035 | 2.166 ± 0.368 |

Values are expressed as mean ± SEM.

accumulation, with a ratio of 2.04 ± 0.15 between the tumor and healthy leg. Tumor-selective uptake of $^{18}$F-FDG, compared with corresponding healthy tissue, was statistically significant ($P < 0.05$ and $<0.005$, respectively) in the 143B and the SaOS-2/Caprin-1 cell line–derived intratibial osteosarcoma models. The ratio of $^{18}$F-FDG uptake between tumor and healthy leg was significantly higher in 143B (3.8-fold) than in SaoS-2/Caprin-1 tumor models (2-fold), whereas the difference between the ratio in the 143B and LM8 tumor models (2.2-fold) did not reach significance (Fig. 1B). The sensitivity of in vivo intratibial osteosarcoma tumor localization by $^{18}$F-FDG–based PET, defined by the number of mice with detectable tumors divided by the total number of animals analyzed, was 100% in the 143B (4/4 mice) and SaOS-2/Caprin-1 (5/5) cell line–derived models and only 50% (3/6) in the LM8 model (Table 2).

*$^{18}$F-FMISO.* $^{18}$F-FMISO, an indicator of hypoxia, accumulated significantly in 143B and SaOS-2/Caprin-1 tumors ($P < 0.01$ and $<0.005$, respectively) and to a lesser extent in LM8 tumors (Fig. 1A). SUV ratios between the tumor and healthy legs were 1.99 ± 0.15 for 143B and 2.23 ± 0.24 for SaOS-2/Caprin-1 models. Both were significantly higher ($P < 0.01$) than the respective ratio in the LM8 model (1.18 ± 0.08) (Fig. 1B). The sensitivity of $^{18}$F-FMISO was high in all 3 mouse models, reaching 100% of tumor-detectable mice in the 143B (15/15) and SaOS-2/Caprin-1 (5/5) osteosarcoma mouse models and 86% (6/7) in the LM8 mouse model (Table 2).

*$^{18}$F-Fluoride.* $^{18}$F-fluoride uptake into the tumors, indicating bone remodeling, differed strongly among the 3 osteosarcoma mouse models (Fig. 1A). In the osteolytic 143B model, $^{18}$F-fluoride uptake in primary tumors did not differ from the uptake of the healthy control leg, and tumor tissue was detectable in 7 of 15 mice (sensitivity, 47%; Table 2). The osteoblastic LM8 model

displayed a higher $^{18}$F-fluoride uptake in the tumor leg than in the healthy leg, with a sensitivity of 87.5% (7/8). The most pronounced tumor uptake was detected in the highly osteoblastic SaOS-2/Caprin-1 model and was significantly higher than in the healthy leg ($P < 0.05$). The analysis of the ratios between tumor and control SUVs confirmed the visual examination: SUV ratios between the tumor and the control legs were 2.28 ± 0.39 in the SaOS-2/Caprin-1 model, 1.32 ± 0.15 in the LM8 model, and 1.08 ± 0.13 in the 143B model. The differences in SUV ratios were significant between SaOS-2/Caprin-1 and LM8 ($P < 0.05$) and between SaOS-2/Caprin-1 and 143B ($P < 0.01$) (Fig. 1B).

### Histologic and Immunohistochemical Validation of PET Imaging Results

In previously reported studies, it has been demonstrated that Ki67, a nuclear marker for cell proliferation, correlates with $^{18}$F-FDG uptake in various tumors (*24–26*). Because we also had a significant correlation between $^{18}$F-FDG uptake and Ki67 in our 3 models (Supplemental Fig. 2A), we used this marker to confirm the presence of active proliferating tumor cells. We observed that the 143B model, which has the highest ratio between tumor and control leg uptake, also showed a high percentage of Ki67-stained cells in the tumor section (Fig. 2A). In the LM8 model, we noticed that Ki67-stained cells were present only in isolated areas of the primary tumor (Fig. 2B), confirming the results from the PET imaging where the $^{18}$F-FDG uptake ratio between the tumor and healthy leg was lower than in the 143B tumor model. Finally, in sections of SaOS-2/Caprin-1 tumors a lower proportion of cells was stained for Ki67, which is also in line with the lowest $^{18}$F-FDG uptake ratio, compared with the other 2 models (Fig. 2C). These observations were confirmed by quantification of the Ki67 positivity on primary tumor sections of the 3 osteosarcoma mouse

## TABLE 2
### Detection Power of PET Imaging

| Tracer | Mouse model | Sensitivity (%) | Mice... With detectable tumors | Total |
|---|---|---|---|---|
| $^{18}$F-FDG | Osteolytic (143B) | 100 | 4 | 4 |
| | Osteoblastic (LM8) | 50 | 3 | 6 |
| | Osteoblastic (SaOS-2/Caprin-1) | 100 | 5 | 5 |
| $^{18}$F-FMISO | Osteolytic (143B) | 100 | 15 | 15 |
| | Osteoblastic (LM8) | 86 | 6 | 7 |
| | Osteoblastic (SaOS-2/Caprin-1) | 100 | 5 | 5 |
| $^{18}$F-Fluoride | Osteolytic (143B) | 47 | 7 | 15 |
| | Osteoblastic (LM8) | 87.5 | 7 | 8 |
| | Osteoblastic (SaOS-2/Caprin-1) | 100 | 4 | 4 |
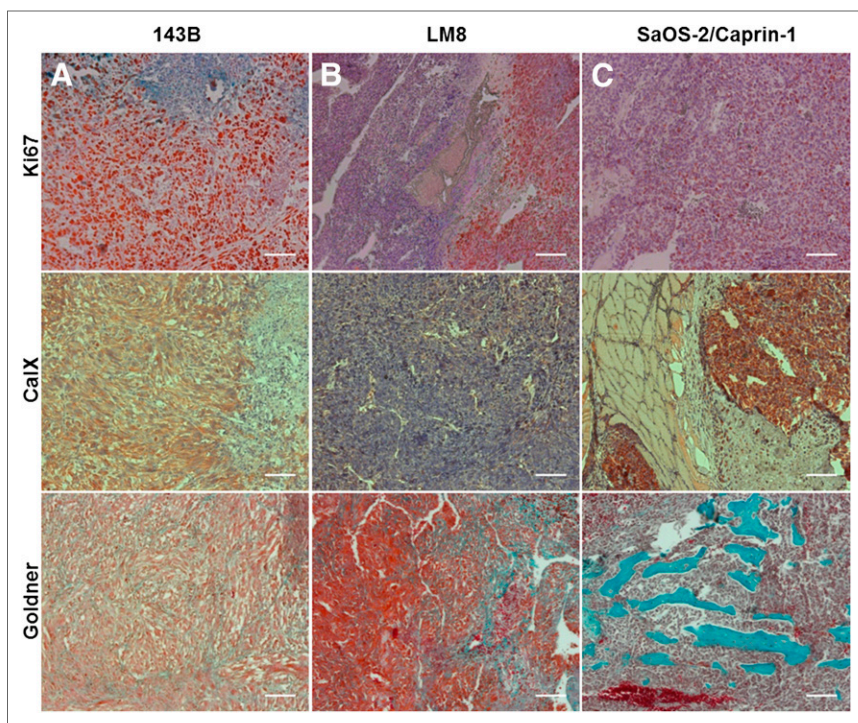
**FIGURE 2.** Combined immunohistochemical and histologic analysis of intratibial primary osteosarcoma tissue in indicated mouse models. Proliferating cells were visualized by Ki67 immunostaining (A), hypoxic tumor areas were identified by immunostaining for CaIX (B), and Goldner trichrome staining indicated osteoid in red and mineralized bone in blue (C). Scale bars, 100 μm.

## DISCUSSION

To develop more selective treatment approaches in osteosarcoma, it could be beneficial for the patient to characterize the biologic phenotype of an individual osteosarcoma in more detail through imaging and accordingly optimize treatment by targeting crucial cellular processes that are most prominent. This will help to reduce the use of ineffective therapy, side effects, and costs (27,28).

Imaging tools such as x-rays and CT scanning give an accurate diagnosis of bone tumors, including osteosarcoma; however, they do not have prognostic value because anatomic changes of tumor size are visible earliest after several cycles of chemotherapy. Therefore, the tumor shrinkage is not considered as a reliable criterion of tumor response to chemotherapy (1). PET imaging, on the other hand, has already been proven to be more sensitive as a prognostic indicator in several cancers (7,9,29). Concerning the diagnosis, the use of a combination of different PET tracers that target different metabolic processes will be a big step forward for gaining additional information about the biology of individual tumors in patients diagnosed with the same type or subtype of osteosarcoma.

models (Supplement Fig. 2B). Indeed, the 143B primary tumor shows a significantly higher percentage of Ki67-positive cells than do primary tumor sections of the SaOS-2/Caprin-1 mice.

Hypoxic conditions in primary osteosarcoma tumor tissue suggested by $^{18}$F-FMISO PET were verified by immunohistochemical staining of tumor sections for CaIX. CaIX is a rapidly and stably upregulated target of hypoxia-inducible factor 1α and therefore a well-established marker of hypoxia. A significant correlation was found between the $^{18}$F-FMISO uptake and CaIX staining in our study (Supplemental Fig. 3A). We also observed a significant difference between the percentage of CaIX-stained cells in the LM8 model, compared with the other 2 models (Supplemental Fig. 3B), relating to the results of the PET imaging. The LM8 model showed the lowest CaIX expression in primary tumor tissue (Fig. 2B), corresponding to the low accumulation ratio for $^{18}$F-FMISO. In contrast, in tumor sections of the 143B and SaOS-2/Caprin-1 models comparable high levels of CaIX expression could be observed (Figs. 2A and 2C), which is in agreement with the high uptake of $^{18}$F-FMISO in these 2 osteosarcoma models.

Fluoride accumulation in bone is a reliable indicator of bone-mineralization, which can be histochemically detected by Goldner trichrome staining. The section of the osteolytic 143B tumor showed low tumor cell production of immature bone, so-called osteoid, and mineralized bone (Fig. 2A). More osteoid and mineralized bone lacking an organized structure was observed in the mildly osteoblastic LM8 model (Fig. 2B). The SaOS-2/Caprin-1 cell line–derived tumors had the highest content of bone-like structures formed by the tumor cells (Fig. 2C). These findings were in good agreement with the results of the $^{18}$F-fluoride PET because SaOS-2/Caprin-1 model showed the highest uptake ratio between the tumor and control leg.

In this study, we investigated this hypothesis in osteosarcoma mouse models with well-characterized histologic phenotypes: osteolytic (143B), slightly osteoblastic (LM8), and strongly osteoblastic (SaOS-2/Caprin-1). A strict comparison between human osteosarcoma types and these mouse models cannot be made. Nevertheless, we can infer that the 143B osteolytic model may reflect the telangiectatic type of osteosarcoma (30). This type shows indeed lytic lesions that are comparable to the ones observed in the 143B mouse model. The LM8 and SaOS-2/Caprin-1 models are considered conventional osteosarcoma because of the formation of dense bony structures at the tumor site. Importantly, our mouse models generate a dominant osteoblastic tumor, which is not observed in human conventional osteosarcoma that typically shows a mixture of lytic and blastic lesions. Differences in the LM8 and SaOS-2/Caprin-1 models that are not observed to the same extent in human disease include the difference in size of primary tumors (smaller in average in the LM8 model), the speed of tumor growth (3 wk for the LM8, compared with 2–4 mo for the SaOS-2/Caprin-1 model), and the degree of mineralization, as we concluded from our study. However, the differences in primary tumor phenotypes observed in the individual animal models likely represent so far nondiagnosable tumor characteristics that contribute to human conventional osteoblastic osteosarcoma. We selected 3 different PET tracers that mark different biologic processes, usually altered in osteosarcoma development: $^{18}$F-FDG, an indicator of glucose metabolism; $^{18}$F-FMISO, an indicator of hypoxia; and $^{18}$F-fluoride, an indicator of bone remodeling.

In a previous pilot study, we also tested $^{18}$F-fluorothymidine, $^{18}$F-fluorocholine, and $^{18}$F-fluoroethyltyrosine in all 3 models. However, the results were inconclusive because of a lack of

reproducibility for each tracer in individual mice of the same model. Therefore, these tracers were not further evaluated in the present study. We included the data of the pilot study in the supplemental data.

We were able to show that the uptake of the individual tracers correlated well with the phenotype assessed by postmortem histology and immunohistochemistry of the primary tumors. The 2 related processes of glucose metabolism—visualized by ^{18}F-FDG tumor uptake—and cell proliferation—as shown by intense Ki67 staining—were predominant in the 143B osteolytic tumor model. Moreover, large areas of hypoxia, which were marked by ^{18}F-FMISO uptake, were noticed in the osteoblastic SaOS-2/Caprin-1 and osteolytic 143B models, perhaps correlating to a higher grade of hypoxia-related chemoresistance, compared with the LM8 osteoblastic model. In the latter model, ^{18}F-FMISO uptake was modest also because of a smaller tumor volume measured in these mice. Immunohistochemistry performed with the CaIX (a marker of hypoxia) confirmed the results obtained by PET imaging.

Finally, ^{18}F-fluoride uptake was consistent with an osteoblastic phenotype. The increased uptake of ^{18}F-fluoride in respective tumors strongly depended on the extent of osteoid and mineralized bone produced by the tumor cells, which was confirmed by histology.

Our findings are in agreement with the work of Hsu et al. who recently characterized 3 prostate cancer mouse models with osteolytic, osteoblastic, and mixed-bone lesions using ^{18}F-FDG and ^{18}F-fluoride PET imaging during tumor progression (31). This study shows that in the LAPC-9 osteoblastic model, ^{18}F-fluoride and ^{18}F-FDG uptake increases over time whereas the PC-3 osteolytic model shows only a progressively higher ^{18}F-FDG uptake. The results presented here are also in line with those of a clinical multitracer PET imaging study in soft-tissue sarcoma reported by Eary et al. (10). This study showed that changes in tumor phenotypes in individual patients in response to treatment can be monitored by consecutive PET imaging on the same day with ^{11}C-thymidine, ^{18}F-FMISO, and ^{11}C-verapamil. These reports indicated that multitracer PET imaging can be used for noninvasive, prognostic characterization of tumor phenotypes complementary to routine histologic analysis of tumor biopsies. Along these lines, new therapeutic strategies focusing on targeting glucose metabolism, hypoxia, and osteoclast differentiation or bone resorption have been investigated in several tumors and also in osteosarcoma (2,32–34). Thus, patients with tumors exhibiting a high ^{18}F-FDG uptake, which are considered aggressive and fast growing (such as the osteolytic phenotype), may in the future benefit from a supplementary antimetabolic therapy. Accordingly, high ^{18}F-FMISO uptake might become indicator for the treatment of predominantly hypoxic and chemoresistant tumors as we observed in osteolytic and slowly growing osteoblastic tumors. Finally, ^{18}F-fluoride uptake will highlight the status of mineralization of the tumor. Hence osteoblastic tumors with high to medium ^{18}F-fluoride uptake and osteolytic tumors showing low ^{18}F-fluoride uptake will need a specific treatment with novel drugs that selectively target, respectively, the formation of new bone or the destruction of it (2,34). Despite the promising results presented in this study, the preclinical models possess certain limitations because they do not reflect the human disease with a mixed osteolytic and osteoblastic phenotype. Further, the PET imaging was performed only when the tumor was at a later stage, which at the same time allowed us to visualize better the differences among the different phenotypes by SUV analysis. PET kinetic modeling with arterial input functions will allow significance to be reached already at earlier time points (35). Compartment modeling will in addition provide information on tracer uptake mechanisms, distinguishing the contributions of tracer extraction from blood and trapping mechanisms within the tissue.

Future preclinical studies need to address the real benefit of the mentioned therapeutic strategies using the PET results of tumor characterization combined with the standard protocol, with the final aim of increasing the survival rate of osteosarcoma patients.

Moreover, clinical experiments need to be performed to define whether there is a correlation among the different osteosarcoma types and a specific pattern of ratios of the 3 tracers that we investigated in this study.

## CONCLUSION

We have evaluated a new potential application of PET imaging for the visualization and characterization of phenotypic features of osteosarcoma primary tumors, making use of preclinical animal models of osteosarcoma. The tumors in each mouse model showed in vivo a distinct pattern of tracer uptake when ^{18}F-FDG, ^{18}F-FMISO, and ^{18}F-fluoride were used. In this way, information about different metabolic processes was obtained. Importantly, these patterns correlated with the histologic characterization of the tumors ex vivo. Taken together, the data presented here support the idea that PET is a useful analytic tool for gaining information on tumor characteristics. These insights will contribute to the design of improved tumor phenotype–tailored therapies, with the final aim of increasing the survival rate of osteosarcoma patients.

## DISCLOSURE

## ACKNOWLEDGMENTS

## REFERENCES

1. Hogendoorn PC, Athanasou N, Bielack S, et al. Bone sarcomas: ESMO clinical practice guidelines for diagnosis, treatment and follow-up. *Ann Oncol.* 2010;21 (suppl 5):v204–v213.
2. Akiyama T, Dass CR, Choong PF. Novel therapeutic strategy for osteosarcoma targeting osteoclast differentiation, bone-resorbing activity, and apoptosis pathway. *Mol Cancer Ther.* 2008;7:3461–3469.
3. Marina N, Gebhardt M, Teot L, et al. Biology and therapeutic advances for pediatric osteosarcoma. *Oncologist.* 2004;9:422–441.
4. Bielack SS, Carrle D, Hardes J, et al. Bone tumors in adolescents and young adults. *Curr Treat Options Oncol.* 2008;9:67–80.
5. Bielack SS, Kempf-Bielack B, Delling G, et al. Prognostic factors in high-grade osteosarcoma of the extremities or trunk: an analysis of 1,702 patients treated on neoadjuvant cooperative osteosarcoma study group protocols. *J Clin Oncol.* 2002;20:776–790.

6. Chen K, Chen X. Positron emission tomography imaging of cancer biology: current status and future prospects. *Semin Oncol.* 2011;38:70–86.

7. Weber WA, Ott K, Becker K, et al. Prediction of response to preoperative chemotherapy in adenocarcinomas of the esophagogastric junction by metabolic imaging. *J Clin Oncol.* 2001;19:3058–3065.

8. Benz MR, Czernin J, Allen-Auerbach MS, et al. FDG-PET/CT imaging predicts histopathologic treatment responses after the initial cycle of neoadjuvant chemotherapy in high-grade soft-tissue sarcomas. *Clin Cancer Res.* 2009;15:2856–2863.

9. Kim DH, Kim SY, Lee HJ, et al. Assessment of chemotherapy response using FDG-PET in pediatric bone tumors: a single institution experience. *Cancer Res Treat.* 2011;43:170–175.

10. Eary JF, Link JM, Muzi M, et al. Multiagent PET for risk characterization in sarcoma. *J Nucl Med.* 2011;52:541–546.

11. Brenner W, Bohuslavizki KH, Eary JF. PET imaging of osteosarcoma. *J Nucl Med.* 2003;44:930–942.

12. Franzius C, Bielack S, Flege S, et al. Prognostic significance of ^{18}F-FDG and ^{99m}Tc-methylene diphosphonate uptake in primary osteosarcoma. *J Nucl Med.* 2002;43:1012–1017.

13. Imam SK. Review of positron emission tomography tracers for imaging of tumor hypoxia. *Cancer Biother Radiopharm.* 2010;25:365–374.

14. Li Y, Wang H, Tu C, et al. Role of hypoxia and EGF on expression, activity, localization and phosphorylation of carbonic anhydrase IX in MDA-MB-231 breast cancer cells. *Biochim Biophys Acta.* 2011;1813:159–167.

15. Knowles HJ, Schaefer KL, Dirksen U, et al. Hypoxia and hypoglycaemia in Ewing's sarcoma and osteosarcoma: regulation and phenotypic effects of hypoxia-inducible factor [abstract]. *BMC Cancer.* 2010;10:372.

16. Yang QC, Zeng BF, Dong Y, et al. Overexpression of hypoxia-inducible factor-1α in human osteosarcoma: correlation with clinicopathological parameters and survival outcome. *Jpn J Clin Oncol.* 2007;37:127–134.

17. Eschmann SM, Paulsen F, Reimold M, et al. Prognostic impact of hypoxia imaging with ^{18}F-misonidazole PET in non-small cell lung cancer and head and neck cancer before radiotherapy. *J Nucl Med.* 2005;46:253–260.

18. Langsteger W, Heinisch M, Fogelman I. The role of fluorodeoxyglucose, ^{18}F-dihydroxyphenylalanine, ^{18}F-choline, and ^{18}F-fluoride in bone imaging with emphasis on prostate and breast. *Semin Nucl Med.* 2006;36:73–92.

19. Sabile AA, Arlt MJ, Muff R, et al. Caprin-1, a novel Cyr61-interacting protein, promotes osteosarcoma tumor growth and lung metastasis in mice. *Biochim Biophys Acta.* 2013;1832:1173–1182.

20. Arlt MJ, Banke IJ, Walters DK, et al. Lacz transgene expression in the subcutaneous Dunn/LM8 osteosarcoma mouse model allows for the identification of micrometastasis. *J Orthop Res.* 2011;29:938–946.

21. Sabile AA, Arlt MJ, Muff R, et al. Cyr61 expression in osteosarcoma indicates poor prognosis and promotes intratibial growth and lung metastasis in mice. *J Bone Miner Res.* 2012;27:58–67.

22. Alf MF, Wyss MT, Buck A, et al. Quantification of brain glucose metabolism by ^{18}F-FDG PET with real-time arterial and image-derived input function in mice. *J Nucl Med.* 2013;54:132–138.

23. Mumprecht V, Honer M, Vigl B, et al. In vivo imaging of inflammation- and tumor-induced lymph node lymphangiogenesis by immuno-positron emission tomography. *Cancer Res.* 2010;70:8842–8851.

24. Yamamoto Y, Nishiyama Y, Ishikawa S, et al. Correlation of ^{18}F-FLT and ^{18}F-FDG uptake on PET with Ki-67 immunohistochemistry in non-small cell lung cancer. *Eur J Nucl Med Mol Imaging.* 2007;34:1610–1616.

25. Shimoda W, Hayashi M, Murakami K, et al. The relationship between FDG uptake in PET scans and biological behavior in breast cancer. *Breast Cancer.* 2007;14:260–268.

26. Walter F, Federman N, Apichairuk W, et al. ^{18}F-fluorodeoxyglucose uptake of bone and soft tissue sarcomas in pediatric patients. *Pediatr Hematol Oncol.* 2011; 28:579–587.

27. Costelloe CM, Macapinlac HA, Madewell JE, et al. ^{18}F-FDG PET/CT as an indicator of progression-free and overall survival in osteosarcoma. *J Nucl Med.* 2009;50:340–347.

28. De Maeseneer DJ, Lambert B, Surmont V, et al. 18-fluorodeoxyglucose positron emission tomography as a tool for response prediction in solid tumours. *Acta Clin Belg.* 2010;65:291–299.

29. Terasawa T, Dahabreh IJ, Nihashi T. Fluorine-18-fluorodeoxyglucose positron emission tomography in response assessment before high-dose chemotherapy for lymphoma: a systematic review and meta-analysis. *Oncologist.* 2010;15:750–759.

30. Klein MJ, Siegal GP. Osteosarcoma: anatomic and histologic variants. *Am J Clin Pathol.* 2006;125:555–581.

31. Hsu WK, Virk MS, Feeley BT, et al. Characterization of osteolytic, osteoblastic, and mixed lesions in a prostate cancer mouse model using ^{18}F-FDG and ^{18}F-fluoride PET/CT. *J Nucl Med.* 2008;49:414–421.

32. Wilson WR, Hay MP. Targeting hypoxia in cancer therapy. *Nat Rev Cancer.* 2011;11:393–410.

33. Jones NP, Schulze A. Targeting cancer metabolism: aiming at a tumour's sweet-spot. *Drug Discov Today.* 2012;17:232–241.

34. Dass CR, Choong PF. Zoledronic acid inhibits osteosarcoma growth in an orthotopic model. *Mol Cancer Ther.* 2007;6:3263–3270.

35. Siddique M, Frost ML, Blake GM, et al. The precision and sensitivity of ^{18}F-fluoride PET for measuring regional bone metabolism: a comparison of quantification methods. *J Nucl Med.* 2011;52:1748–1755.